Progress in Photovoltaics: Research and Applications

WILEY

PROGRESS IN PHOTOVOLTAICS

RESEARCH ARTICLE OPEN ACCESS

Nonuniformity of Irradiation Distribution on Vehicles' Bodies

Evgenii Sovetkin[1] | Michael Gordon[1] | Neel Patel[1,2] | Andreas Gerber[1] | Angèle Reinders[2] | Robby Peibst[3] | Bart E. Pieters[1]

[1]IMD-3, Photovoltaik, Forschungszentrum Jülich GmbH, Jülich, Germany | [2]Energy Technology, Eindhoven University of Technology, Eindhoven, The Netherlands | [3]Institute for Solar Energy Research Hamelin (ISFH), Emmerthal, Germany

Correspondence: Evgenii Sovetkin (e.sovetkin@fz-juelich.de)

Received: 27 June 2024 | **Revised:** 22 October 2024 | **Accepted:** 18 November 2024

Funding: This work was funded by the Helmholtz Data Federation (HDF) by providing services and computing time on the HDF Cloud cluster at the Jülich Supercomputing Centre (JSC) [51]. Furthermore, this work was funded by the Gauss Centre for Supercomputing e.V. (www.gauss-centre.eu) by providing computing time through the John von Neumann Institute for Computing (NIC) on the GCS Supercomputer JUWELS at Jülich Supercomputing Centre (JSC). This work is supported by the HGF project "Living Lab Energy Campus (LLEC)", as well as the "Street" project (Street — Einsatz von hocheffizienten Solarzellen in elektrisch betriebenen Nutzfahrzeugen, Förderkennzeichen: 0324275A).

Keywords: GIS | irradiation inhomogeneity | vehicle integrated photovoltaic

ABSTRACT

Nonuniformity of irradiation in photovoltaic (PV) modules causes a current mismatch in the cells, which leads to energy losses. In the context of vehicle-integrated PV (VIPV), the nonuniformity is typically studied for the self-shading effect caused by the curvature of modules. This study uncovers the impact of topography on the distribution of sunlight on vehicle surfaces, focusing on two distinct scenarios: the flat-surface cargo area of a small delivery truck and the entire body of a commercial passenger vehicle. We employ a commuter pattern driving profile in Germany and a broader analysis incorporating random sampling of various road types and locations across 17,000 km^2 in Europe and 59,000 km^2 in the United States using LIDAR-derived topography and OpenStreetMap data. Our findings quantify irradiation inhomogeneity patterns shaped by the geographic landscape, road configurations, urban planning, and vegetation. The research identifies topography as the primary factor affecting irradiation distribution uniformity, with the vehicle's surface orientation and curvature serving as secondary influencers. The most significant variation occurs on vertical surfaces of the vehicle in residential areas, with the lower parts receiving up to 35% less irradiation than the top part of the car. These insights may be used to improve the design and efficiency of vehicle-integrated photovoltaic systems, optimizing energy capture in diverse environmental conditions.

1 | Introduction

Vehicle-integrated photovoltaics (VIPV) represent a pioneering approach in photovoltaic application, seamlessly incorporating solar modules into the structure of various vehicles. For passenger electric vehicles, VIPV technology can reduce reliance on grid-based charging systems, diminishing the need for frequent plug-in sessions [1, 2]. VIPV provides continuous cooling of the cargo for refrigerated cargo trailers even during prolonged parking [3]. VIPV may even supply most energy required to propel more efficient lightweight vehicles such as cargo bicycles [4–6].

The efficacy of VIPV systems is intricately linked to the surrounding environment, significantly impacting performance by both natural and built elements [7–14]. The shadows cast by vegetation vary with climate, and architectural styles and the width of streets influence shadows from buildings. Hence, estimates of yield losses due to shading cannot be expressed as a single constant number but rather as a function depending on a geographical location and type of road, with values having a significant variation. The dependency on a vehicle's location and driving patterns makes yield predictions and the financial viability of VIPV a complex and challenging topic, underscoring the need for further research and development in this area.

This study delves into a critical aspect of VIPV performance: the uniformity of irradiation distribution across the vehicle's body. Variations in module irradiance, precipitated by partial shading or the inherent curvature of the vehicle's surface, can lead to significant electrical losses. These losses originate from the current mismatch of serially connected and nonuniformly irradiated cells. To address this problem, an adaptation of the interconnection topology to the curvature was proposed previously [15], where a module is divided into parallel subgroups containing cells with similar azimuth and elevation angles toward the sun.

The impact of irradiance distribution on curved modules has been investigated in various works [16–19]. For example, [16] employs a curve-correction factor derived from ray-tracing simulations to model the irradiation on curved surfaces. Several works focus on modeling irradiance in urban environments using LIDAR-derived topography data (e.g., [8, 9, 20–23]). However, to our knowledge, the specific challenge of irradiation distribution across curved modules on vehicles in natural settings remains unaddressed in the existing literature.

Moreover, how topography impacts the amount of light on the surface contributes to the light nonuniformity, as surface points higher from the ground surface tend to receive larger irradiation values as more sky is visible [9, 24, 25]. Furthermore, for the same reason, the vehicle sides closer to buildings tend to be darker than the opposite sides. These effects have not been quantified previously in the literature. Furthermore, the comparison of the impact on nonuniformity originated the surface curvature and topography is yet to be studied.

To study average nonuniformity patterns across VIPV modules, we employ our simulation tool, SSDP [26], to model the irradiance distribution on the vehicle's body, utilizing high-resolution LIDAR-based digital surface models (DSMs) to replicate topographical features accurately. Our study employs two strategies for placing a car. In the first approach, we use a measurement dataset for the time and locations of a small flat-surface cargo vehicle. In the second strategy, using the complete body of a commercial vehicle, we perform simulations in various places around Europe and the United States and study the influence of geographical location and road type on the annual irradiation distribution on the vehicle's body.

The outline of the paper is as follows: Section 2 reviews the data utilized for our simulations. Section 3 describes our simulation pipeline and lists the limitations of our approach. Section 4 highlights the main results for the flat- and curved-surface vehicle and the computational requirements needed to reproduce our simulations.

2 | Data

This paper utilizes several sources of data to achieve its goals. To perform irradiance simulations, we use high-resolution LIDAR data to describe topography (see Section 2.1) and satellite-based irradiance data to model the sky (see Section 2.2). Section 2.3 overviews the two measurement campaigns with the dataset containing irradiance and vehicle position. That data are used to verify our simulation model and provide an example of the driving profile. To identify roads and sample points on them, we use OpenStreetMap (OSM) (see Section 2.4). Lastly, Section 2.5 describes how the shape of the commercial vehicle body is sampled.

2.1 | Topography Data

High-resolution topography data are often published as LIDAR cloud points. This type of data consists of a list of coordinates (x, y, z) and additional data (e.g., point color). With sufficient density, the point cloud provides an accurate three-dimensional shape for the objects. In contrast, DSM topographies give a so-called 2.5-dimensional topography. Such regular rasters provide processing speed benefits. And since one of our focuses is global-scale simulations, we restrict our work to the DSM raster data.

We resample LIDAR data as described in [24, 25] to obtain the DSM raster. For this work, we use rasters with a pixel size of $0.5 \times 0.5\,\mathrm{m}^2$, and we work with maximum- and minimum-statistic rasters for the publicly available LIDAR data in Europe and the United States. Our complete data covers the area of $300{,}000\,\mathrm{km}^2$ ($100{,}000\,\mathrm{km}^2$ Europe, $200{,}000\,\mathrm{km}^2$ United States). In terms of storage, the sampled raster data require 12.5 TB. Table 1 summarizes the sources of data we use. Figure 1 depicts an example of the high-resolution DSM, where a small portion of a village with houses and trees is visible. The left part of Figure 1 shows the raster with the maximum statistic, and the right part of Figure 1 shows the minimum statistic raster with all trees and other vegetation absent.

In this paper, we manually select specific regions of interest that contain large urban centers, mountain settlements, and various climatic zones. We utilize only approximately 25% of the data available [24]. However, such an approach is more targeted toward more populated regions and thus more relevant to VIPV. Table 2 describes the bounding boxes and the corresponding areas with a total area of over $75{,}000\,\mathrm{km}^2$.

In Germany, we consider 13% of the North Rhine-Westphalia (NRW) state, which contains large cities such as Köln, Düsseldorf, Wuppertal, and Duisburg. In Luxembourg, we include the capital and small towns around it in the country's southern portion. We consider alpine and valley regions in Switzerland, including Lausanne and Lake Neuchâtel. In France, we had no access to large metropolitan areas. There, we consider two areas in the Region Auvergne-Rhône-Alpes, with Aurillac and Ambérieu-en Bugey being the most populous towns. Due to LIDAR data availability in Spain, we only use areas in the northern part of Spain, with Bilbao being the largest city. In the United States, we consider the complete island of Hawai'i, San Jose, and San Francisco

TABLE 1 | Publicly available LIDAR data sources.

Country	Citation	Country	Citation
USA	[27]	Switzerland	[28]
Germany, NRW	[29]	France	[30]
Germany, Berlin	[31]	Spain	[32]
Luxembourg	[33]	The Netherlands	[34]

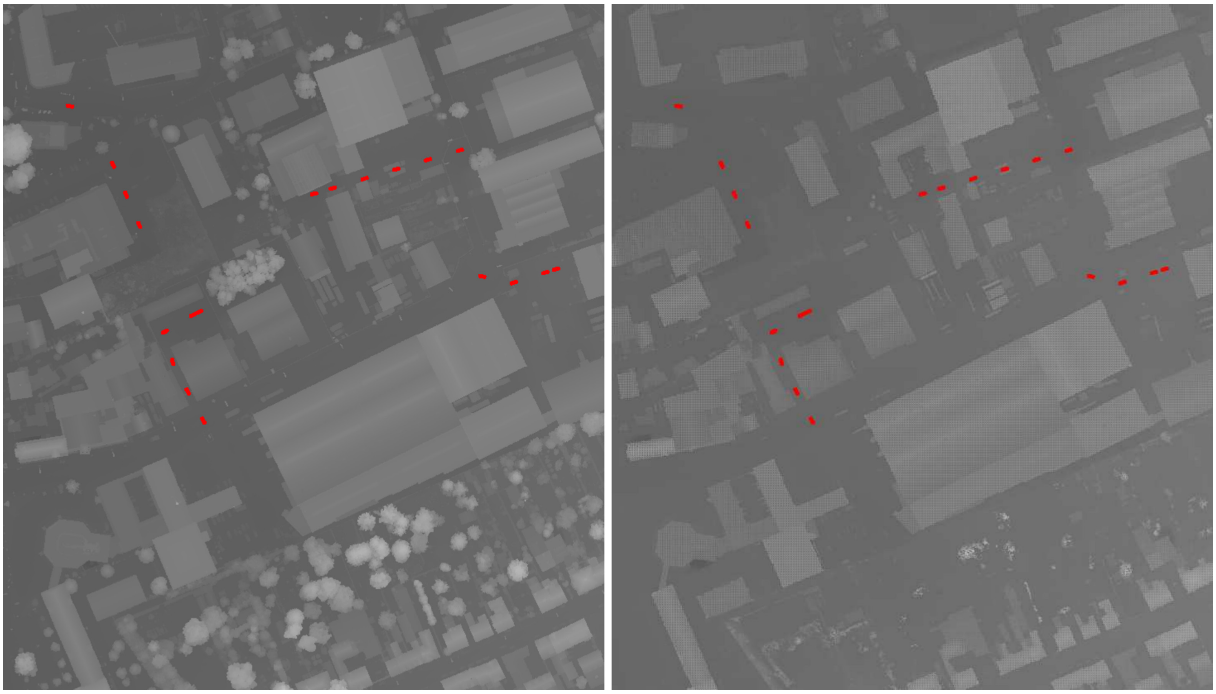

FIGURE 1 | Examples of max-statistic (left) and min-statistic (right) rasters with vehicles placed every 20m on the road surface (indicated by red). Sampled positions to place a car are indicated with dashes. The minimum statistic raster has no tree visible. The pixel value intensity (except for the placed vehicles) indicates the elevation: the brighter, the higher.

in the Bay Area, Las Vegas, with its surrounding area in Nevada. In South Dakota, we consider the small town of Buffalo. A large area is considered in Florida, including the city of Orlando. In Georgia, we include Atlanta and Atlantic City in New Jersey. The practical areas in Hawai'i and the Bay area are smaller than those in Table 2, as no simulations are performed for the ocean surface.

2.2 | Satellite Atmospheric Irradiance Data

We use historical atmosphere irradiation data from Copernicus [35]. The service includes ground-level Global Horizontal (GHI) and Diffuse Horizontal irradiance (DHI) data in Europe and Africa with a model that considers cloud coverage. The cloud coverage is estimated from satellite images and thus has low temporal and spatial resolutions: one observation per 10 min and $5 \times 5\,\mathrm{km}^2$ area. For this paper, we collected 11 years of observations in different European locations.

To assess the accuracy of the satellite-based source, we compare the GHI irradiation with 115 weather stations in Germany DWD [36]. The DWD provides data with a temporal resolution of 10 min. Figure 2 (left) depicts the raw observations, where the y-axis shows the GHI value from the weather station, and the x-axis shows corresponding data queried from Copernicus. The two sources' root-mean-square error (RMSE) equals $\approx 90\,\mathrm{W/m}^2$. Such errors are caused by deficiencies in satellite-based models, such as the limited spatial resolution and cloud lens effects [37]. The errors decrease when irradiance is integrated over time. Figure 2 (right) demonstrates the relative error between integrated irradiance computed from the weather station and the Copernicus data computed for different integration periods—even integration periods of 1-year yield relative errors of 3% across various stations.

2.3 | Measurement Data and Model Validation

We utilize vehicle irradiance data from two different measurement campaigns. The data from the first measurement campaign is published in [9], which consists of measurements of four irradiance sensors mounted on a vehicle (facing up, left, right,

TABLE 2 | The total sampling area and corresponding bounding boxes.

Area (km^2)	Bounding box				Name
4865	50.85	6.31	51.56	7.19	Germany, NRW
683	49.56	5.94	49.81	6.28	Luxembourg
2550	46.48	6.53	46.88	7.27	Switzerland
2543	46.67	8.58	47.07	9.32	Switzerland, alpine region
2584	45.67	5.53	46.07	6.27	France, Lyon
1191	44.81	2.38	45.09	2.88	France, Aurillac
2708	43.03	−3.05	43.43	−2.31	Spain, Bilbao
25,416	18.84	−156.08	20.37	−154.66	USA, Hawai'i
13,853	37.20	−122.67	38.17	−121.22	USA, California, Bay Area
2517	35.95	−115.40	36.40	−114.84	USA, Nevada, Las Vegas
131	45.53	−103.62	45.63	−103.47	USA, South Dakota, Buffalo
7921	28.14	−81.92	28.92	−80.99	USA, Florida
7516	33.67	−84.95	34.45	−84.01	USA, Georgia, Atlanta
1774	39.26	−74.75	39.67	−74.30	USA, New Jersey, Atlantic city
Total: 76,251					

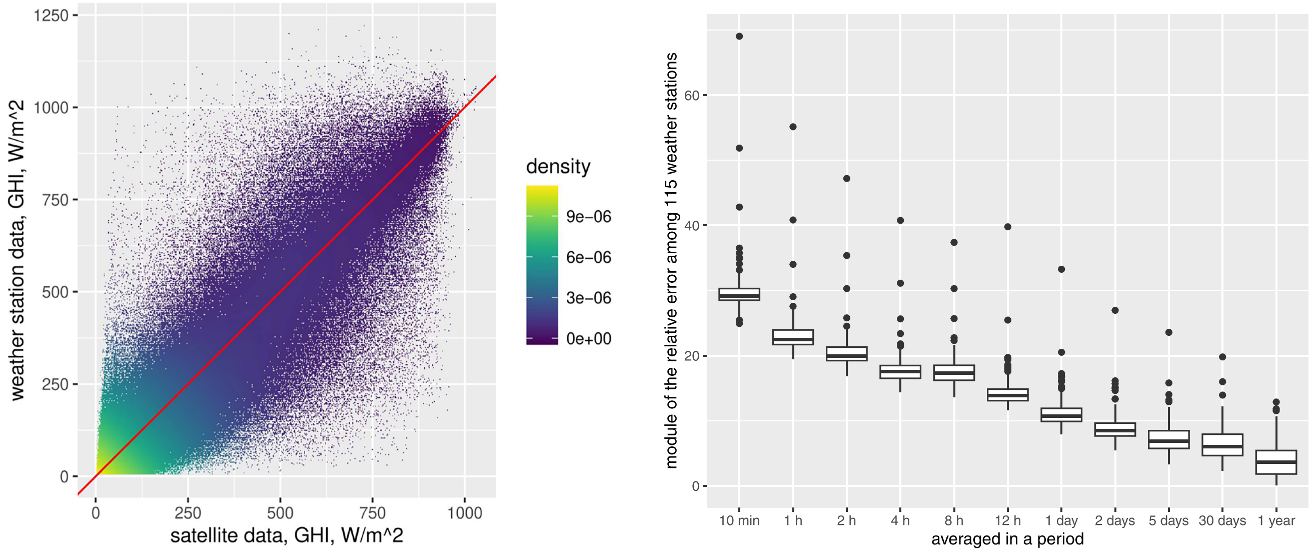

FIGURE 2 | Comparison of 115 weather stations with corresponding satellite-based GHI observations. Left: observed GHI values for weather station and corresponding satellite-based values. Right: distribution of the absolute value of the relative error between integrated irradiance for 115 weather stations and satellite-based observations.

and back). We used measurements collected over 7 months containing 150,000 observations (73 h, distance: 3422 km), where data are only available during the trips (i.e., no data is collected during parking). The second measurement campaign was performed on a different vehicle equipped with a complete PV system comprised of 15 modules [38], with 4×10^6 observations recorded between April and August 2021. The second measurement campaign recorded the data for trips and parking states. The trips exhibit a commuting driving profile. The trip data lasts 81 h (7% of all observations), parking at the office lasts 342 h (31%), and parking at home lasts 684 h (62%). Figure 3a depicts the small delivery truck used in the measurement campaign. The vehicle has four irradiance sensors: the roof, left, and right sensors are located on the top section of the cargo section, and the rear irradiance sensor is positioned in the lower part of the cargo section. For the complete system analysis and analysis of efficiencies from atmospheric irradiation to high voltage battery, see [39].

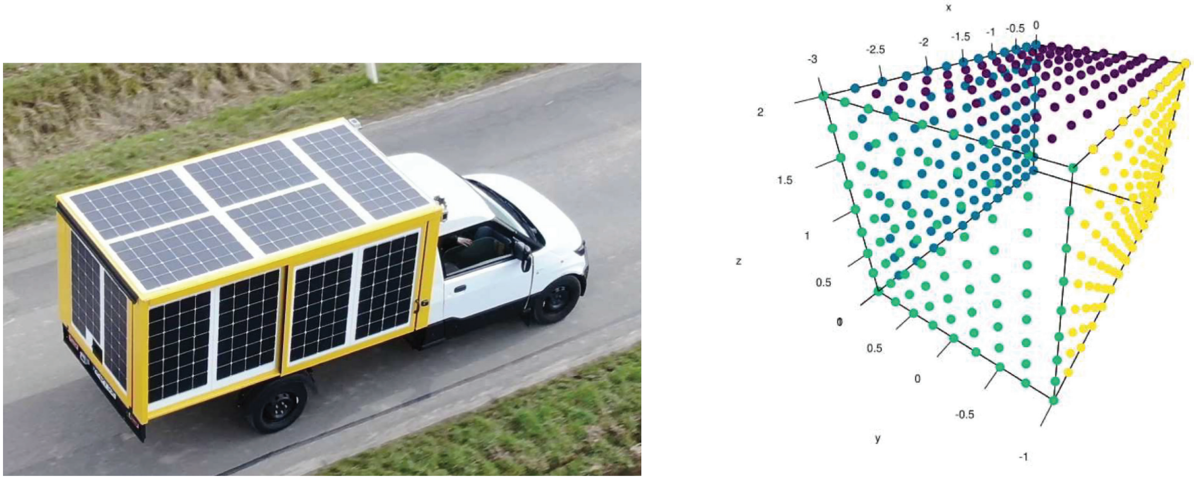

(a)

(b)

FIGURE 3 | Vehicle and its cargo area representation. (a) The vehicle used in the second measurement campaign [38]. (b) A mesh of points representing the sides of the vehicle (resolution 1 point per 25 × 25cm^2).

We integrate irradiance over time to validate our simulations and compare the resulting values with the irradiance sensor data. Tables 3 and 4 give the irradiation values for each side of the vehicle, shown in daily averages (kWh/m^2/24 h) for both measurement campaigns (the first measurement performance reported in [9], the second in [39]). Overall, the median relative error over different sensors equals 6%.

Several factors contribute to the modeling error. First, our data itself have a measurement error. Limitations in GPS accuracy may lead to significant simulation deviations within a dense urban environment. The vehicle's orientation is crucial for modeling the vertically oriented sensors. In the preprocessing stage, we calibrated the magnetic compass and GPS-bearing data to reduce inaccuracies in parking and trip state [9]. Second, the simulation model contains several approximations. We model the sky with a non-isotropic diffused light Perez All-Weather Sky Model [40] computed from GHI and DHI value satellite-based measurements (see Section 2.2). However, this sky model is unaware of the exact locations of clouds in the sky. Thus, the accuracy of the sky intensity distribution depends on weather conditions.

The satellite-based irradiance data source introduces additional errors in the modeling pipeline. Section 2.2 compared ground-based and satellite-based data sources, with RMSE instantaneous observations equal to 90 W/m^2. To estimate the relative contribution of that error in the complete modeling pipeline, we compare that value with the RMSE for the predicted roof irradiance to the measured roof irradiance. For simulations from both measurement campaigns, for 4 million observations, the RMSE equals 200 W/m^2. Hence, the irradiance source contributes 45% of RMSE for instantaneous simulations. For irradiation (integrated irradiance over time), we observe relative errors between sensor reading and simulation model to vary between 3% and 12%. At the same time, Figure 2 (right) demonstrates that integrating ground- and satellite-based data over 1000 h results in a relative error of around 5%.

TABLE 3 | First measurement campaign, daily averages of irradiation (kWh/m^2/24 h), [9].

Sensor	State	Measured	Simulated
Roof	Trip	7.18	6.39
Rear	Trip	4.62	4.79
Right	Trip	2.41	2.58
Left	Trip	3.95	3.71

Note: Observations from March to October 2021.

TABLE 4 | Second measurement campaign, daily averages of irradiation (kWh/m^2/24 h), [38, 39].

Sensor	State	Measured	Simulated
Roof	Trip	5.63	5.84
Roof	Office	7.57	6.97
Roof	Home	8.48	8.31
Rear	Trip	1.58	1.30
Rear	Office	3.51	3.31
Rear	Home	3.64	3.54
Right	Trip	2.25	2.20
Right	Office	5.83	4.44
Right	Home	1.95	2.07
Left	Trip	1.73	1.69
Left	Office	1.61	2.06
Left	Home	4.11	3.91

Note: Observations from April to August 2021.

2.4 | OSM Data

OSM is a collaborative and open-source mapping platform. OSM consists of geospatial information about the world collected and contributed by a global community of volunteers. This information includes details about roads, buildings, landmarks, and other features found on a map.

The maps are represented through three basic elements: “nodes,” “ways,” and “relations.” The node elements represent individual geographical points and are used as individual features (landmarks, mountain peaks, individual trees) or as part of other elements. The way elements are ordered lists of nodes, allowing them to represent objects such as buildings (closed ways) or streets. Lastly, the relation elements describe more complex features, including nodes, ways, and other relations.

Every element in OSM has a list of attributes called tags. Tags are key-value pairs assigned to nodes, ways, and relations, providing specific information about an object. For example, a tag on a road might include information about its name, surface type, and maximum speed limit. In contrast, a building tag might contain information about its use, number of floors, and architectural style. All the roads in OSM are annotated as ways with the tag key “highway.” The corresponding tag value indicates the type of road.

In OSM, roads are classified by their performance (maximum speed allowed for vehicles) and function. Table 5 describes the most commonly occurring roads in our sampled dataset. Not every road can be used by cars (e.g., footway, path, and cycleway), and the most common type of roads, “track,” is only used by agricultural machinery.

The OSM road classification is used to categorize locations as urban or non-urban. For instance, “residential,” “service,” and “living street” can be considered urban environments, whereas “track,” “tertiary,” “primary,” and “secondary” roads are located outside towns and form non-urban environments.

We download the OSM data in two files for Europe and the United States from the GeoFabrik service [42]. The files are processed by splitting them into small chunks, each describing a bounding box with a side of 0.5°. Each file contains an additional 0.25° of the data around it. The files are stored in OSM portable binary format (PBF), optimized for efficient data storage. The files contain primitive blocks containing the OSM elements data, indexed with the header. Such structured files make it

TABLE 5 | OSM road classification for most commonly occurring roads.

Tag value	Sampled length (km)	Description
Track	27,600	Minor land-access roads that are not considered part of the general-purpose road network (e.g., paths through agriculture fields).
Residential	22,600	Roads that provide access to, or within, residential areas but which are not normally used as through routes.
Service	19,600	Used for vehicle access to a building, service station, industrial estate, business park, beach, campsite, etc.
Path	11,800	Used by pedestrians, small vehicles like bicycles, for animal riding or livestock walking.
Unclassified	10,000	Minor public roads, typically at the lowest level of whatever administrative hierarchy is used in that jurisdiction.
Tertiary	8000	Roads connecting smaller settlements and within large settlements for roads connecting local centers.
Footway	7100	Minor pathways which are used mainly or exclusively by pedestrians.
Secondary	4500	Roads that are not part of major routes but nevertheless form a link in the national route network.
Primary	3200	Major highway linking large towns, but which does not satisfy the performance requirements of a motorway.
Motorway	1800	The highest performance roads within a territory.
Cycle way	1200	Implies that the route is designated for bicycles.
Trunk	1100	High-performance or high-importance roads that do not meet the requirements for motorway but are not classified as primary (country-specific).
Living street	950	Type of roads have lower speed limits, and special traffic and parking rules compared to streets tagged using residential.

Note: The total length of sampled roads 125,000 km (see Section 3.2), [41].

possible to access the data quickly and efficiently without reading the entire file. In terms of storage, we use 153 GB of storage for all OSM data used here.

2.5 | Vehicle Body

A set of points approximates the surface of a vehicle's body. Each point consists of five coordinates: three-dimensional body coordinates and two-dimensional angles of the normal vector. For the flat-surface cargo body, we use a set of points, as depicted in Figure 3b.

We use freely available models from [43] for the three-dimensional shape of a curved vehicle. In particular, we downloaded a blender-formatted file and manually processed it in the blender software [44]. During the manual processing, only the vehicle's outer shell was preserved. After that, the shape was exported to an OBJ file for further processing. Figure 4 depicts the rendering of the data in the OBJ file. Next, we randomly sample the surface, generating a list of five-dimensional points (Figure 4, right). This information is enough to model irradiance on a vehicle's body's curved surface.

Our vehicle body preprocessing pipeline could be improved. Some points in the right part of Figure 4 are dark due to an unusual normal vector orientation. This happens on the edge of a body part, where the concept of the normal direction is not uniquely defined. However, in this paper, this is not a problem, as we study only the general trends in the body's irradiation distribution and do not apply any functions that combine multiple body points.

3 | Approach

Algorithm 1 shows the steps of our simulation pipeline. The input for the pipeline is provided in Step 1 and depends on the type of simulations we perform. For the flat-surface body simulations, we set P to be the set of 432 points shown in Figure 3b and road locations L to be the measured GPS location and car orientation. In the curved-body simulations, the set P is obtained by sampling the three-dimensional car model and road locations from the OSM data to get the L (see Section 3.2). In Step 2 of Algorithm 1, the road locations are clustered together to form raster bounding boxes. This step ensures sufficient topography data for location in every direction. The generated bounding boxes are processed in the loop (Steps 3–5). Iterations of the loop are independent and computed in parallel on several machines.

Step 4 in Algorithm 1 shifts the vehicle body coordinates P to each of the simulation locations L_B. Here, we assume that the points in L_B are positioned in the middle of the road, and we place the vehicle on the right side of that location, aligning with the driving side in continental Europe. Step 5 in Algorithm 1 varies depending on the type of simulations conducted. For flat-surface body simulations, irradiance simulations are performed for each recorded GPS time and vehicle location. In the case of curved-surface body simulations, we compute irradiation with the integrated sky.

Step 7 in Algorithm 1 aggregates the simulation results. In flat-surface body simulations, the results are reported as average irradiance ($\mathrm{W/m^2}$) over all available observation points. For curved-surface body simulations, the results yield irradiation ($\mathrm{Wh/m^2}$), and we normalize these values to obtain relative GHI/notopo irradiation (a dimensionless quantity, detailed in Section 3.1).

In the following sections, we dive into the details of the critical steps of Algorithm 1. The core tool of simulations is our open-source irradiance modeling C library, SSDP [26], which runs simulations in Step 5. Section 3.1 reviews the irradiance modeling approach and its most time-critical places. The other steps in Algorithm 1 consist of processing data for SSDP input and output. One of the critical sections of those preparations is sampling road locations in different countries and on various types of roads (Section 2.4). Our procedure is described in detail in Section 3.2. Lastly, in Section 3.3, we discuss the limitations of our simulation approach.

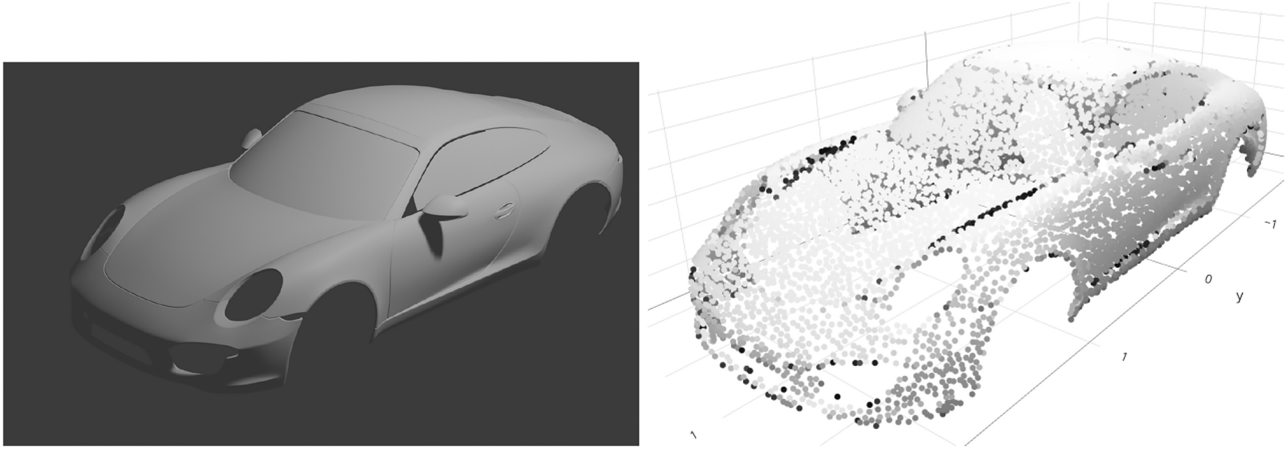

FIGURE 4 | A vehicle body used in simulations. Left: rendered OBJ file. Right: 10,000 points sampled from the surface represented by OBJ. Every point contains information about the surface normal. The color of the points corresponds to the irradiation level: the higher the irradiation, the brighter the point.

Algorithm 1 Body irradiance simulation pipeline.

```
Input: 5-dimensional coordinates $P$ describing the body (Section 2.5), road location coordinates $L$ (see road sampling procedure in Section 3.2), $D = 500m$ minimum required topography distance.
cluster road locations $L$ into bounding boxes $\{B\}$ so that every road location in $B$ is at least $D$ meters away from the edge of the bounding box.
for (each bounding box $B$ with road locations $L_B$) do
    Generate a set of observation points by shifting $P$ to each location in $L_B$. Total number of observation points equals $|P||L_B|$. The vehicle's origin is located in the middle of the left side. In this way, the car will be placed on the right side of the road (on the driving side in continental Europe).
    query a list of DSM rasters that describe the topography and perform irradiance simulations (see details in Section 3.1). The simulation results are written in HDF5 files.
end for
Aggregate irradiance values for different locations from all HDF5-files.
Output: Average irradiance ($W/m^2$) on the flat-surface body cargo vehicle, grouped by trips and parking state. Average relative GHI/notopo irradiation on the complete passenger vehicle body computed for different locations and road types.
```

3.1 | Modeling Irradiance

Typically, to model the irradiation at a given point on a tilted surface, one must estimate the intensity of irradiation coming from various directions. For that, one must model the sky (sun position and diffused light), shading from the surrounding topography, and reflections from the ground. In other words, the sky is projected on a surface with a given position and orientation, yielding the plane-of-array irradiance, I_{PoA}, for each observation point. The I_{PoA} consists of several components:

$$I_{\mathrm{PoA}} := I_{\mathrm{direct}} + I_{\mathrm{diffused}} + I_{\mathrm{ground}},$$

where I_{direct} is the direct light from the sun, I_{diffused} is the diffused light, and I_{ground} is the light that comes from the ground. The I_{direct} is non-zero when the sun is visible to the observer and is determined using observer orientation, sun position, and the horizon around the observer. The I_{diffused} light consists of all visible sky patches and results from the sky model. The ground component I_{ground} has a simplified model of the light reflected from the ground. We take the light from sky patches obstructed by the horizon and scale the resulting value with the albedo parameter [0,1]. For a curved surface, we assume its smoothness and model irradiation on the corresponding tangent plane, ignoring any light originating from below it. We refer the reader to [9] for more details. SSDP irradiation modeling can be intuitively understood as a single-reflection ray-tracing, and this approach is also implemented in similar models such as "r.sun" [45] and "Solar Analyst" [46]. Although a complete ray-tracing approach may be more accurate, it is too computationally intensive for the VIPV setting.

In SSDP, we use the Perez All-Weather model [40] for the sky, where the complete sky dome is modeled from Global Horizontal (GHI) and Diffuse Horizontal (DHI) irradiance values, allowing us to take into account different weather conditions. For the solar position, we use the freeSPA algorithm [47]. The sky can be aggregated at several time points to form an integrated sky. Figure 5 shows the integrated sky in the northern Netherlands (latitude and longitude: 53.2, 6.70) and in the north of Spain (latitude and longitude: 43.28, −2.91). Here, we used satellite irradiance data for over 11 years.

In order to represent topography, we use regularly spaced rasters with DSM, which are more efficient to navigate than unstructured meshes. Topography is important for computing the horizon, which helps model shading caused by the environment at each simulation location. The horizon shows the profile of obstacles around the observer, and identifies parts of the sky covered by topography. This is an essential step in calculating the amount of light reaching the surface of interest. From the computational point of view, due to the amount of data required to represent topography, horizon computation also takes a significant amount of the simulation time. Therefore, in [24, 25], we proposed a new quasi-Monte Carlo-inspired approximate horizon algorithm. This approach reduced the computation of the horizon by 2–4 times, significantly bringing down simulation costs for the whole irradiance modeling. In particular, our implementation allowed us to use a large topography raster, combine many simulations, and reduce overheads on other computation parts. In our pipeline, we routinely use rasters that represent 16-km^2 topography and have 64-MP resolution. Furthermore, we guarantee that every point of interest sees at least 500 m of topography in each direction.

Elements of topography may not only cover the sky but also be the source of light through reflections. In SSDP, we model reflections by uniformly distributing diffused light over the visible topography. This simple approach is much more straightforward and computationally faster than the ray-tracing methods. In all simulations of this paper, we assume a constant albedo of 0.2.

When doing simulations for many nearby points, storing them in a spatial index is beneficial. Such caching reduces horizon computations for closely positioned points and sky initialization for points with similar orientations.

The output of simulations is given either in irradiance (with units $\mathrm{W/m^2}$) for instantaneous simulations or irradiation (with units $\mathrm{Wh/m^2}$) for simulations integrated over time. We use two different normalization strategies for time-integrated irradiation to obtain relative irradiance. In the first strategy, normalization is computed by dividing every point on the vehicle by the corresponding integrated GHI value. Over 11 years, this amounts to 12.59 $\mathrm{MWh/m^2}$. We refer to this normalization as "GHI" normalization.

The second normalization, "notopo," is obtained by first computing irradiation distribution on the vehicle in the environment without topography. For that, we use 360 different directions for the car and average the resulting irradiation over all directions. As in other simulations, we use the albedo value of 0.2. For every point of the vehicle, we divide irradiation by the corresponding value of the irradiation without the influence of topography. The

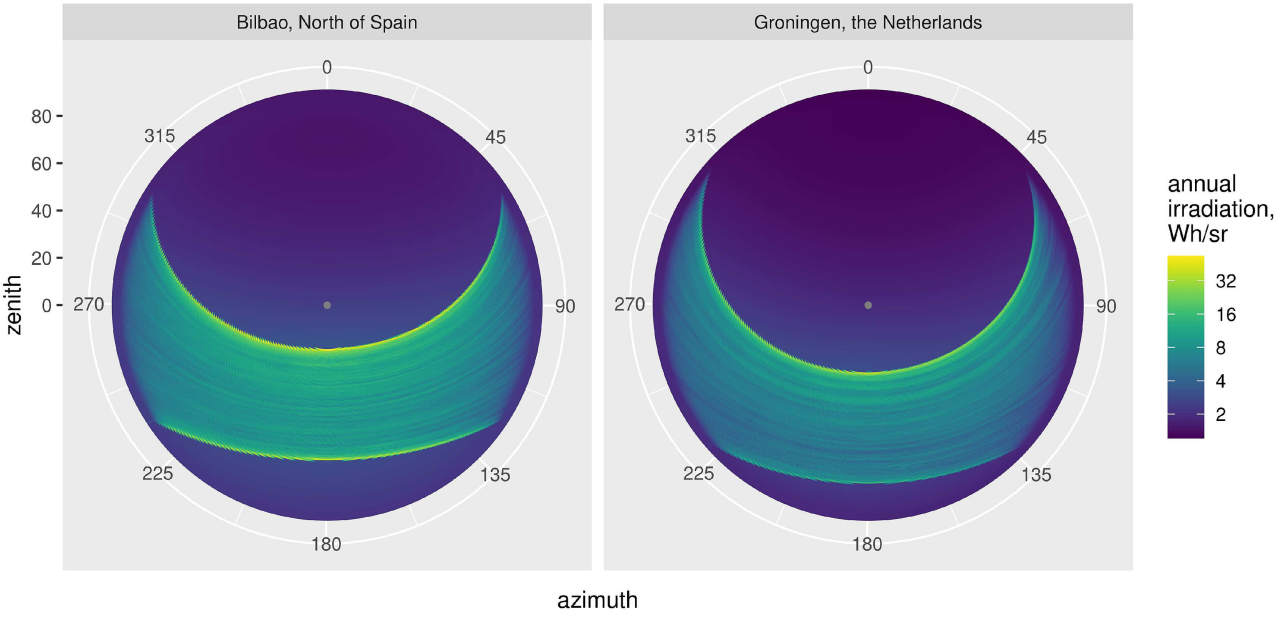

FIGURE 5 | Eleven-year integrated sky. Left: Bilbao, North of Spain. Right: Groningen, the Netherlands (right). Each point color shows the average over 11 years of irradiation for each sky location, Wh/sr.

"notopo" normalization allows us to factor out the effects of the irradiation due to the zenith angle or the curvature of the surface. In other words, it isolates the losses purely attributed to the topography.

The normalization methods "notopo" and "GHI" for horizontal surfaces produce the same results. In both cases, the normalized values are expected to fall between 0 and 1. However, these values can exceed 1. An example of this would be a scenario where a vehicle is positioned on roads inclining toward the north in the northern hemisphere. In such a situation, the vehicle's roof, facing south, may absorb more solar radiation than what is measured as GHI irradiation, resulting in normalized values on the roof exceeding 1 for both normalization methods. Nonetheless, given the comprehensive sampling and averaging of irradiation across various road directions, it is reasonable to anticipate that our normalized values will consistently fall within the 0 to 1 range. Consequently, we refer to the normalized values as "relative GHI/notopo irradiation." We define "relative GHI/notopo losses" by calculating one minus the relative irradiation. Both metrics are dimensionless and can be expressed as percentages.

Relative GHI losses account for environmental influences like topography and transposition losses, which result from the angle of a surface. On the other hand, relative notopo losses are only considered topography losses. As a result, relative notopo irradiation is typically higher on vertical surfaces than relative GHI irradiation. Moreover, the discrepancy between relative GHI and relative notopo losses directly reflects the transposition losses.

3.2 | Sampling Roads in OSM

We aim to gather a representative sample of lighting conditions across various road types mentioned in Table 2. To achieve this, we select samples from different kinds of roads based on their frequency of occurrence. For each road type, we then sample vehicle locations to encompass the range of possible lighting conditions.

Our sampling method is detailed as follows: For each OSM PBF file, which represents a square of approximately 0.75 degrees on each side, we uniformly select 10,000 roadway identifiers (IDs) tagged as "highway." For every chosen road, we perform linear interpolation between its nodes and position virtual vehicles at intervals of 20 m along the direction of the road. While road lengths vary, the average road length sampled within a single OSM PBF file tends to stabilize due to the law of large numbers as the quantity of sampled road IDs increases. Figure 1 depicts an example of a raster with a vehicle placed regularly on a selected road. The total length of roads considered is $\approx$ 125,000 km.

3.3 | Limitations

Our simulation approach has several limitations, which we list in this section. The first set of limitations originates from the way we simulate irradiance. First, we use a simple ground reflection model and ignore any variation in albedo value for different locations or seasons [48]. Throughout simulations, we use a constant albedo of 0.2, which, for example, underestimates reflections in the desert area of Nevada or snow-covered roads in South Dakota.

Second, we ignore the self-shading of the car, for example, shadows caused by the side-view mirrors. At the same time, this simplified model allows the modeling of generic vehicle shapes, where a sufficient number of points can be used to approximate arbitrary surfaces.

Our primary focus for curved-surface vehicles is identifying variations in irradiation caused by differences in local topographies. Therefore, throughout the simulations, we use the integrated sky computed for a fixed location in Europe. We intentionally do this to factor out the influence of the solar angle at various locations, make irradiance depend only on the topography, and ignore effects related to the local sun trajectories and local weather patterns. The used sky is unrealistic for more southern latitudes (e.g., Hawai'i, Florida, California, and Spain), as the sun draws different trajectories in the sky (see Figure 5), and local weather differences also play a role in the diffused sky patterns. Therefore, our results should be used only for comparative studies of the effects of architectural styles and vegetation types. In Section 4.4, we compare simulations in Spain for correct local sky settings, where we demonstrate that correct sun trajectory has only a minor impact on the relative irradiation (on average, 4% more relative irradiation).

Our simulations study the average irradiation, allowing us to compare it on different types of roads and locations. However, one needs to work with instantaneous irradiance values to model PV electrical output and the electrical losses caused by irradiance inhomogeneity. To extend the study to PV electrical output, several additional variables must be included in the analysis: module dimensions and cell arrangement, cell interconnection, cell type, and PV module temperature model. Nevertheless, the annual irradiation profile can be used to estimate the potential energy losses for time-integrated PV yield approximately. The scope of this paper is a study on variation in nonuniformity for different road types and several locations, and we leave detailed PV yield modeling for future works.

Another set of limitations comes from the geospatial data we use. The OSM data has limited information on the width of the roads. We do not use this information at all and always place the vehicle so that its left side lies in the middle of the road. We acknowledge that on wide roads with many lanes in each direction, the irradiation distribution might be different on different lanes. We also ignore any one-way streets in the city, which might place the vehicles in unnatural directions. However, we don't expect any biases in average irradiation here.

Our curved-surface vehicle simulations use OSM data to place vehicles inside LIDAR-based topography. Those two data sources might have a relative bias from one to another. These situations should be rare, as we have not seen examples with large deviations.

4 | Results

Here, we consider simulation results for the flat-surface cargo and the curved-surface vehicles. For the flat surface vehicle in Section 4.1, we study the average irradiance on the vehicle's body for recorded vehicle driving patterns. We look at parking (home and office locations) and trips (for two different measurement

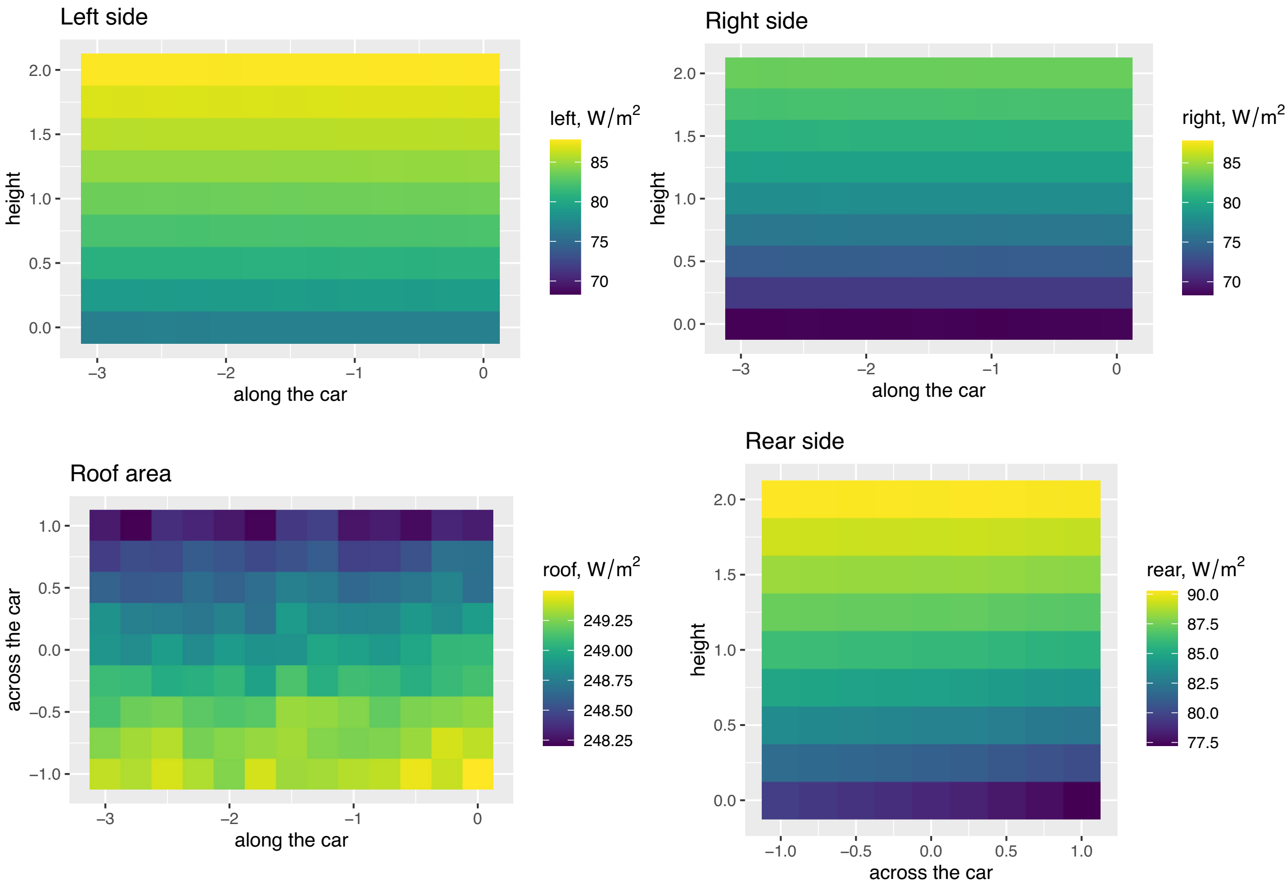

FIGURE 6 | Average irradiance computed over all trips during the second measurement campaign. The areas correspond to the mesh shown in Figure 3b.

campaigns) and report results in average irradiance values with units of W/m^2. Section 4.2 takes a more global sampling approach for a curved-surface vehicle with simulations using an integrated sky irradiation. The simulations are reported as relative irradiation values, indicating the percentage of the irradiation or the losses. We study the influence of geographical location in Section 4.3 and the impact of height, vegetation, and sky in Section 4.4. Lastly, Section 4.5 elaborates on the computational requirement and simulation reproducibility.

4.1 | Flat-Surface Small Cargo Vehicle

Figure 6 presents the average irradiation distribution around different parts of the vehicle (measured in watts per square meter, W/m^2) during the second measurement campaign. The analysis reveals that the irradiation levels on the right and left sides of the car are uniform in the horizontal direction. Overall, the right side is 7% dimmer than the left side. The average irradiation intensity on the roof varies slightly between 248 and 249 W/m^2, with the right side being marginally dimmer than the left by 0.5%. The car's rear side shows a slightly nonuniform distribution horizontally, where the bottom right is approximately 5% dimmer than the bottom left. In comparison, during the first measurement campaign, the left received between 81 and 100 W/m^2, and the right received 72 and 89 W/m^2. Roof irradiance was observed to range from 230 to 232 W/m^2.

The parking at home location in the second measurement campaign is parallel to the road. The average irradiance on the left side ranges between 65 and 87 W/m^2, and on the right, ranging between 135 and 163 W/m^2. The average irradiance on the car's rear side ranges between 140 and 170 and is slightly darker than the right. The average irradiance on the roof ranges between 345 and 353 W/m^2. The parking in the office location is similar to the parking at home, with the only difference on the right side being darker than the left.

The particular driving profile highly impacts the values of the average irradiance. In our measurement campaigns, there is a time-dependent bias in the direction of travel. The first measurement campaign starts at a fixed location in the morning and goes in different directions, mainly in the southwest direction from the starting point. The second measurement campaign is a strictly commuter pattern, where a person drives northeast to their office in the morning and southwest in the afternoon. Overall, a general pattern is observed in all considered data: There is a 10% decrease in irradiance for every meter drop of

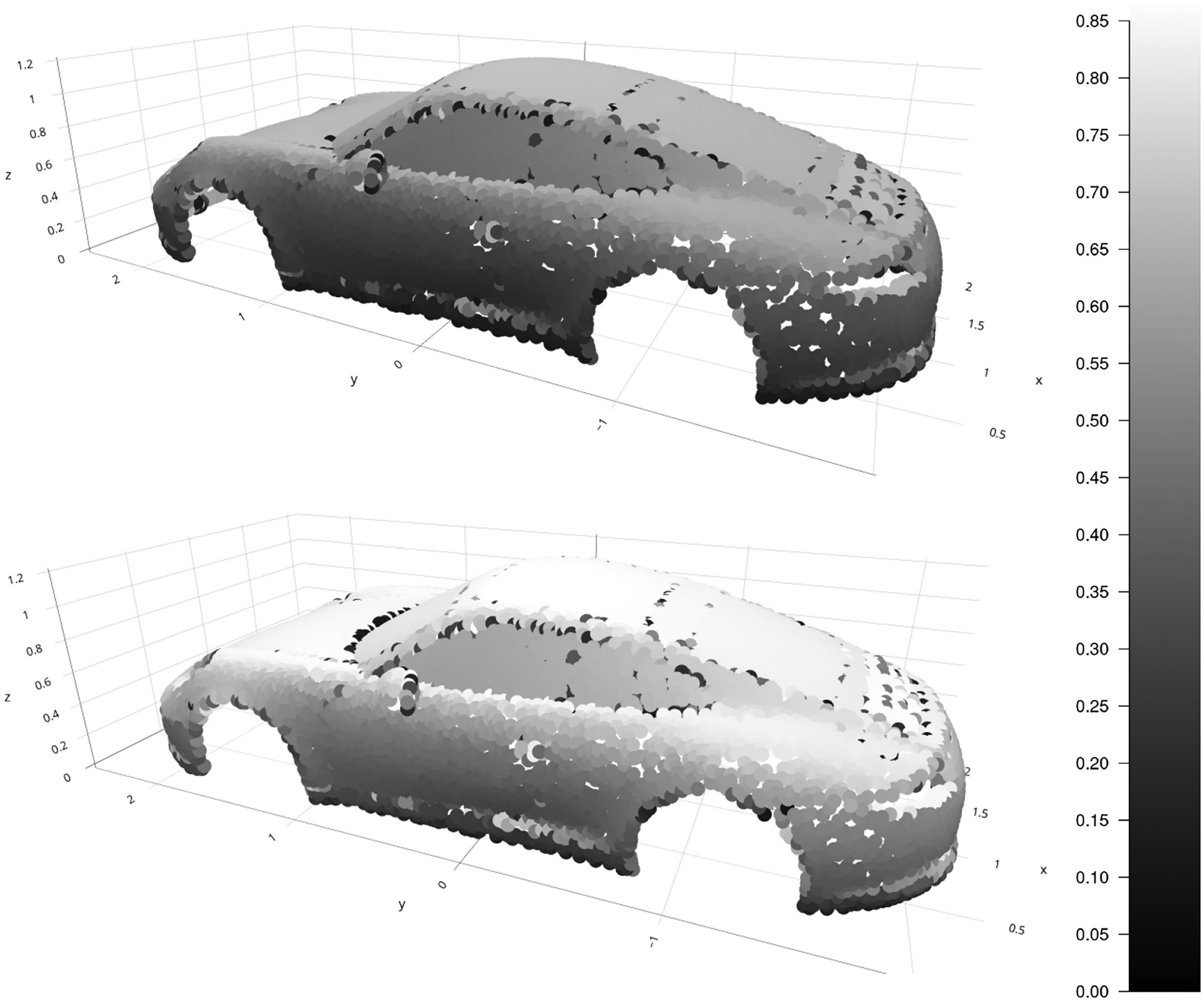

FIGURE 7 | Relative GHI irradiation (normalization that includes transposition losses). Top: residential roads. Bottom: motorways.

elevation above the ground. This is due to the higher elevation above ground, which causes less sky obstruction by surrounding objects.

4.2 | Curved Surface Vehicle

In our simulations for curved-surface vehicles, we employ integrated sky irradiation. We normalize the car's irradiation levels regarding relative GHI/notopo irradiation, as discussed in Section 3.1. Through two distinct normalization methods, we can analyze how losses are distributed between transposition losses (arising from the surface's curvature and angle) and environmental losses (stemming from topography and shading).

Figures 7 and 8 depict the vehicle relative irradiation for two discussed types of normalization (GHI and notopo, respectively) averaged for all considered geographical locations for residential and motorway roads. Each figure comes with a common palette scale, allowing us to compare irradiation on different types of roads. The dark outliers in the scatterplot are deficiencies of our three-dimensional model processing pipeline, explained in Section 2.5. Those outliers do not influence the paper's main results and can be ignored.

Figure 7 demonstrates that residential streets are significantly darker (71% on the roof) compared to the irradiation distribution on motorways (87% on the roof). Furthermore, the irradiation distribution on the vehicle is not uniform, with the general trend

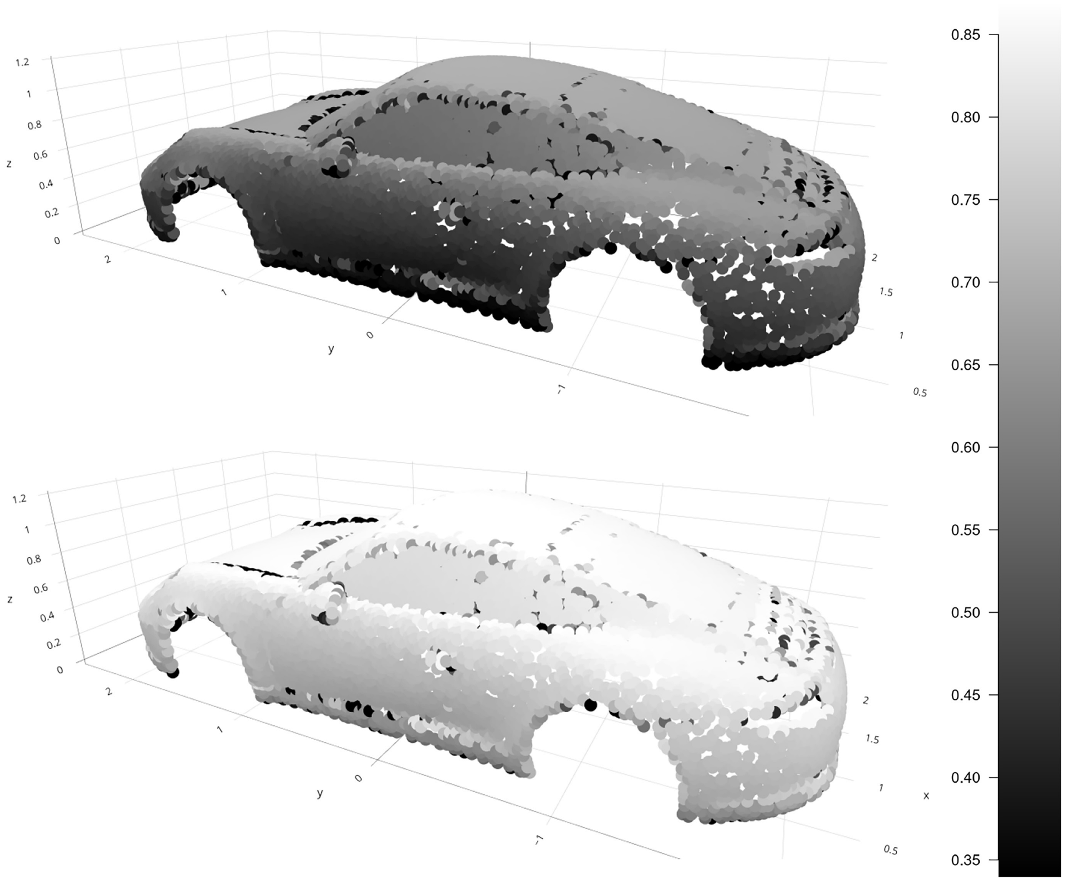

FIGURE 8 | Relative notopo irradiation normalization (no transposition losses). Top: residential roads. Bottom: motorways.

TABLE 6 | Relative GHI/notopo losses (in %) and corresponding transposition losses share (tls, in %).

	Residential			Motorway		
Side	**GHI**	**notopo**	**tls**	**GHI**	**notopo**	**tls**
Roof	29	29	≈ 0	13	13	≈ 0
Window	56	43	21	38	20	47
Lower door	82	60	26	65	34	47
Rear window	34	33	3	16	15	6
Bonnet	32	32	≈ 0	15	14	7

Note: Values are determined from Figures 7 and 8.

for vertical and low surfaces being the darkest. However, this inhomogeneity cannot be entirely attributed to the transposition losses, as Figure 8 exhibits similar irradiation distribution in the vehicle doors. On motorways, the relative notopo irradiation is significantly greater than the relative GHI irradiation, demonstrating a more negligible influence of the topography for motorways. This indicates fewer objects in the surroundings obstruct the sky.

Table 6 summarizes the findings in Figures 7 and 8 regarding the relative irradiation losses. Comparing GHI and notopo normalization, we can conclude that losses due to the environment constitute significant losses for all surfaces. For horizontal surfaces such as the roof, rear window, and bonnet, the transposition losses (GHI losses minus “notopo” losses) do not contribute more than 6% to the total losses. For vertical surfaces (windows and doors), transposition losses range between 21% and 26% on residential roads and up to 47% on motorways.

4.3 | Influence of Geographical Location and Road Types

The results shown in Figures 7 and 8 are averaged over different locations. However, the irradiation also depends on the geographical location, as other countries implement different road construction guidelines and historically adapt different styles of architecture. Furthermore, climate zones affect the type and density of vegetation, which also significantly impacts irradiation. Figure 9 demonstrates this by depicting the boxplot of the relative GHI irradiation of the roof points for vehicles on motorways in different countries. Boxplots in Figure 9 depict the relative GHI irradiation for different points on the roof averaged over simulated locations. The boxplots capture light's nonuniformity, not the irradiation distribution in various geographical locations. Nevada is a clear outlier with only 3% relative losses due to its desert surroundings and large roads within Las Vegas. At the same time, Spain, Luxembourg, Switzerland, and France

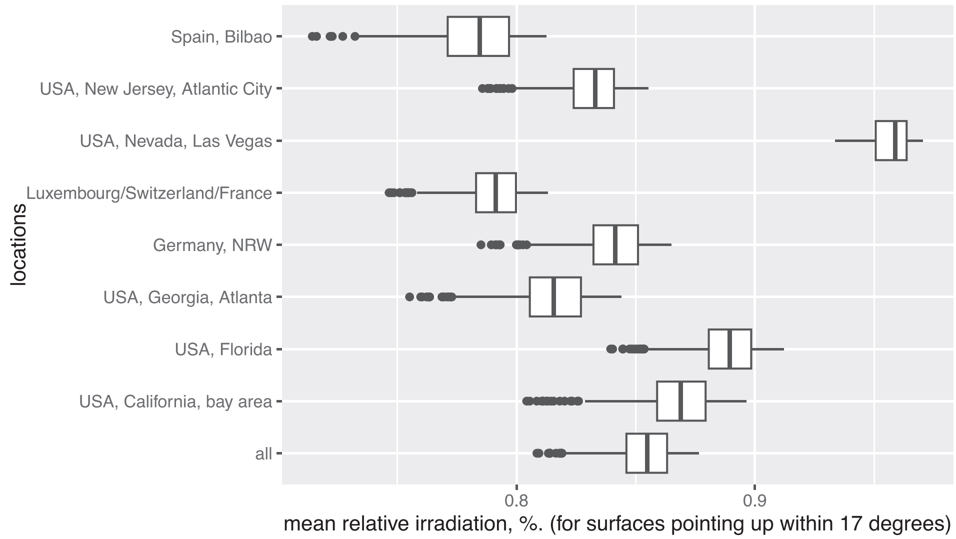

FIGURE 9 | Comparison of relative GHI irradiation on the roof for vehicles on motorways depending on the geographical location. Here, boxplots describe the nonuniformity of light on the roof.

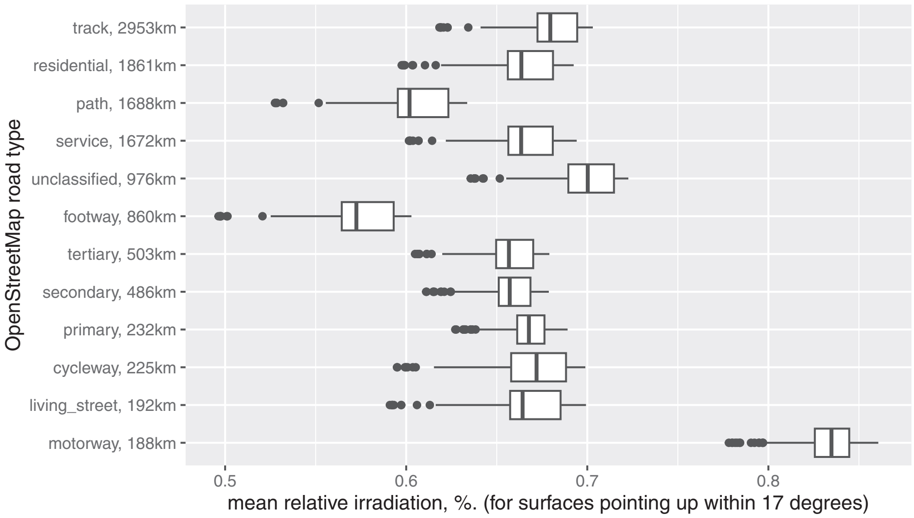

FIGURE 10 | Comparison of relative GHI irradiation on the roof depending on the road type. Here, boxplots describe the nonuniformity of light on the roof. Simulation location: Germany.

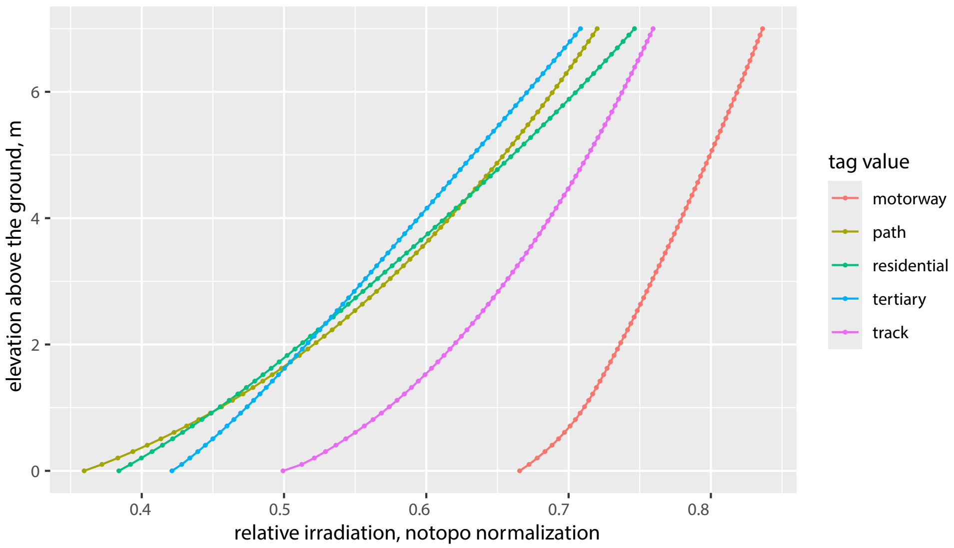

FIGURE 11 | Relative notopo irradiation on the left side of the vehicle depending on the road type.

TABLE 7 | Irradiation losses due to vegetation.

Tag value	Length, km	Vegetation losses
Track	3024	0.15
Residential	1838	0.15
Service	1704	0.15
Path	1691	0.18
Unclassified	967	0.15
Footway	843	0.18
Tertiary	523	0.21
Secondary	494	0.23
Cycleway	227	0.18
Motorway	218	0.08
Primary	206	0.22
Living_street	189	0.13

Note: Simulation location: Germany (see Table 2).

TABLE 8 | Relative error for simulations using two different skies (see Figure 5).

Tag value	Length, km	Relative error, %
Track	2250	3.75
Path	723	2.63
Service	677	3.04
Unclassified	612	2.92
Residential	513	3.64
Tertiary	343	3.35
Footway	339	3.21
Motorway	136	2.19
Secondary	125	3.46
Primary	103	2.94
Cycleway	101	2.82

Note: Simulation location: Spain (see Table 2).

TABLE 9 | Computation time breakdown.

Task	%
Sky transfer initialization	32
Checking cache of computed skies	24
Horizon computation	18
Sampling topography	14
Projecting sky	10
Checking location cache	2

have relative losses on motorways of more than 20%. Figure 9 also indicates that the level of nonuniformity depends on the location. In particular, Spain and Luxemburg have comparable losses, but the standard deviation of the light on the roof is more significant in Spain.

Figure 10 compares vehicle irradiation depending on the road type. Here, we model irradiation on ≈ 12,000 km of roads in Germany, NRW, with boxplots depicting the distribution of light on the vehicle's roof. Among all different road types, "path" and "footway" have the highest average irradiation losses (around 40%), as those roads are very narrow and usually not suitable for cars. The "motorway" has the least irradiation losses of 16%. Other types of roads have losses of around 33%. The distribution of losses is country-dependent; nevertheless, the general trend is that high-performance roads (motorway, trunk, motorway link, trunk link) have the least losses, whereas narrow roads (paths, pedestrian, footway) have the most.

Similarly to the results in Section 4.1, we generally observe a lower irradiance on the right side of the vehicle due to the car being placed on the right side of the road. For example, on "secondary" roads in Germany, the right side is 7% darker than the left side of the vehicle which is the same difference as we observed in Section 4.1.

4.4 | Impact of Height, Vegetation, and Sky

In the curved-surface and flat-surface vehicles, we observed that elevation above the ground is the primary factor influencing the irradiation losses. To investigate this behavior for more significant elevations above the ground, we perform simulations in Germany, where we compute relative irradiation on a vertical surface from 0 to 7 m above the ground. The surface faces left w.r.t. the road direction. Figure 11 shows the relative notopo irradiation depending on the elevation above the ground for different types of roads. The figure demonstrates that irradiation inhomogeneity behavior is also exhibited for elevations higher than 2m, which is relevant for taller vehicles, like trucks.

In all of our simulations so far, we have utilized the maximum statistic from LIDAR point clouds. Switching to the minimum statistic provides a clearer picture of irradiation losses caused specifically by vegetation. Table 7 outlines the extent of losses due to vegetation, calculated as the difference in relative notopo irradiation obtained from the `min`- and `max`-statistic topographies. Motorways show minimal influence from vegetation, with relative notopo irradiation losses at 0.08. Urban road types such as "residential," "service," and "living street" roads, which are typically found within city limits, experience higher vegetation losses, around 0.15. Conversely, major roads like "primary," "secondary," and "tertiary," which are often located in less urbanized areas with abundant trees and vegetation, face even more significant losses, with relative notopo irradiation losses reaching up to 0.22.

We use the single integrated sky (see Figure 5, right) computed for Groningen in the northern Netherlands for all geographical locations. This approach isolates irradiation losses caused by topography and ignores any effects of sun trajectories and local weather patterns. To study the impact of the sky and climate on relative irradiation, we perform simulations using the data available in Spain for integrated sky used in other simulations and the correct local sky (see Figure 5, left). Table 8 shows the relative error between relative irradiation computed for different skies. Due to the significant latitude differences between Spain and the Netherlands, the sun goes on average higher, which results in less shading and, hence, more relative irradiation. However, Table 8 demonstrates that, on average, the sun trajectories and weather climate are marginal and within 4%.

Tables 7 and 8 demonstrate results only for road types with a total sampled length of more than 100 km, corresponding to 5000 sampled vehicle locations (sampling every 20 m for every selected road piece; see Section 3.2).

4.5 | Computational Requirements and Reproducibility

The computation time depends on several factors, including how car locations are sampled, the size of the topography raster, and the computer performance. For our simulations, we use the compute nodes of the JUWELS supercomputer with an Intel Xeon Platinum 8168 CPU processor with 48 cores [49].

In Sections 4.2–4.4, we detail simulations that involved processing irradiation data for 75.09 billion points, necessitating 29,933 CPU hours for computation. This measurement indicates the number of hours a single CPU requires to complete these calculations. The model of the car involved in these simulations is represented by 10,000 points, which translates to simulations being conducted over 7.51 million different vehicle positions. The computational effort amounts to approximately 897 ms per location when running 16 processes in parallel.

From a data storage and retrieval perspective, managing simulations for a million locations entails reading 33 TB of data from the hard disk. This necessitates a minimum storage throughput of 16 megabytes per second (MB/s) to maintain efficiency. Table 9 provides an overview of the time distribution across various stages of the simulation process. According to our findings, a significant portion of the computational time is dedicated to sky simulation computations, an aspect that offers opportunities for optimization in future research endeavors.

We provide software to generate our results reproducibility https://figshare.com/s/13141e26acd3f73c810b [50]. It consists of scripts for sampling points from the vehicle's three-dimensional models, sampling points on OSM roads, and SSDP scripts for simulations. Furthermore, it contains computed data for irradiation distribution for different geographical locations and road types.

5 | Concluding Discussion and Future Work

This study has highlighted the irradiation inhomogeneity across PV modules in VIPV applications. It is established that current mismatches in serially connected cells, induced by uneven irradiance distribution, may significantly constrain the overall yield of PV systems. In the context of VIPV, such losses may be minimized by the design of cell interconnection and on-board electronics. This paper quantified the average annual irradiation distribution on a vehicle body, allowing such VIPV system optimizations and improving VIPV yield forecast models.

This paper demonstrated that the surrounding topography highly impacts irradiation distribution on vehicles and depends on geographical location and the type of road. We have identified distinct nonuniform irradiation patterns primarily attributable to shading dynamics. Specifically, the higher the observer above the ground, the less shading occurs, hence the higher the irradiation. Furthermore, all topographic elements, such as trees and buildings, are closer to the driving side of the car, making the driving side darker.

We demonstrated that topography, not curvature or surface orientation, contributes most to the irradiation losses. In particular, the irradiation distribution along vertical surfaces has a more severe variation than a curved roof. The most significant variation is on the car's sides, with the lower parts receiving up to 35% less irradiation than the top part in residential areas. Most of those losses are attributed to the topography, and transposition losses have a minor share in dense urban environments.

Despite the valuable insights gained from this study, several limitations should be considered. Firstly, we compute annual irradiation patterns with the integrated sky. This approach precludes a detailed analysis of instantaneous irradiance and its electrical implications for PV modules. However, one needs two orders of magnitude of additional storage to model instantaneous irradiance with sky modeled at specific time points. Therefore, our future work will address the storage optimizations of the modeling pipeline for instantaneous irradiance. This would facilitate instantaneous irradiation simulations on the same large scale as we presented in this paper.

Moreover, our nonuniformity simulations are yet to be verified with actual measurements. Our irradiation modeling framework was validated by measuring irradiation with a single sensor for each direction. The challenge of measuring nonuniformity variation is that the measurement error of typical outdoor irradiance sensors is comparable to the expected irradiance variation.

Lastly, the reliance on LIDAR data due to cost and availability constraints limits the geographic scope of our study. To overcome this, we aim to incorporate alternative geospatial data sources, such as satellite imagery or map data, in our modeling efforts. This expansion will enable a more comprehensive analysis across a wider array of geographies.

Author Contributions

Evgenii Sovetkin: conceptualization (lead), software (equal), writing – original draft (lead); writing – review and editing (equal). **Michael Gordon:** software (equal). **Neel Patel:** software (equal). **Andreas Gerber:** funding acquisition (lead). **Angèle Reinders:** writing – review and editing (equal). **Robby Peibst:** data acquisition. **Bart E. Pieters:** software (equal), writing – review and editing (equal).

Acknowledgments

The authors gratefully acknowledge the Helmholtz Data Federation (HDF) for funding this work by providing services and computing time on the HDF Cloud cluster at the Jülich Supercomputing Centre (JSC) [51]. Furthermore, we gratefully acknowledge the Gauss Centre for Supercomputing e.V. (www.gauss-centre.eu) for funding this project by providing computing time through the John von Neumann Institute for Computing (NIC) on the GCS Supercomputer JUWELS at Jülich Supercomputing Centre (JSC). This work is supported by the HGF project "Living Lab Energy Campus (LLEC)", as well as the "Street" project (Street — Einsatz von hocheffizienten Solarzellen in elektrisch betriebenen Nutzfahrzeugen, Förderkennzeichen: 0324275A). Thanks are due to the IBG-3 (FZJ) for providing the vehicle and collecting the data. Open Access funding enabled and organized by Projekt DEAL.

Conflicts of Interest

The authors declare no conflicts of interest.

References

1. A. Kouzelis, "Model-Based Impact Analysis of Vehicle-Integrated Photovoltaics and Vehicle-to-Grid on Electric Vehicle Battery Life" (Master's Thesis, Delft University of Technology, 2022), resolver.tudelft.nl/uuid:f3f716b3-f57e-486b-b5b9-8d5edf643d41.

2. P. Hoth, L. Heide, A. Grahle, and D. Göhlich, "Vehicle-Integrated Photovoltaics: A Case Study for Berlin," *World Electric Vehicle Journal* 15, no. 3 (2024): 113.

3. "Solar Powered Trucks," (2020), tsscgroup.com/products-and-services/truck-bodies-semi-trailers/solar-powered-trucks/.

4. J. Schünemann, S. Finke, S. Severengiz, N. Schelte, and S. Gandhi, "Life Cycle Assessment on Electric Cargo Bikes for the Use-Case of Urban Freight Transportation in Ghana," *Procedia CIRP* 105 (2022): 721–726, The 29th CIRP Conference on Life Cycle Engineering, April 4 -6, 2022, Leuven, Belgium.

5. I. Maranga, G. Burleson, R. Christen, and I. Da Silva, "Design and Testing of a Solar-Powered Bicycle in Nairobi, Kenya," in *International Design Engineering Technical Conferences and Computers and Information in Engineering Conference*, Vol. Volume 2B: 45th Design Automation Conference, (2019).

6. Z. Lin, Q. Hao, B. Zhao, M. Hu, and G. Pei, "Performance Analysis of Solar Electric Bikes," *Transportation Research Part D: Transport and Environment* 132 (2024): 104261.

7. M. C. Brito, T. Santos, F. Moura, D. Pera, and J. Rocha, "Urban Solar Potential for Vehicle Integrated Photovoltaics," *Transportation Research Part D: Transport and Environment* 94 (2021): 102810.

8. D. de Jong and H. Ziar, "Photovoltaic Potential of the Dutch Inland Shipping Fleet: An Experimentally Validated Method to Simulate the Power Series From Vessel-Integrated Photovoltaics," *Solar RRL* 7, no. 8 (2023): 2200642.

9. E. Sovetkin, J. Noll, N. Patel, A. Gerber, and B. E. Pieters, "Vehicle-Integrated Photovoltaics Irradiation Modeling Using Aerial-Based LIDAR Data and Validation With Trip Measurements," *Solar RRL* 7, no. 8 (2023): 2200593.

10. H. Samadi, G. Ala, V. Lo Brano, P. Romano, and F. Viola, "Investigation of Effective Factors on Vehicles Integrated Photovoltaic (VIPV) Performance: A Review," *World Electric Vehicle Journal* 14, no. 6 (2023): 154.

11. H. Samadi, G. Ala, V. L. Brano, P. Romano, and F. Viola, "Investigation of Effective Factors on Vehicles Integrated Photovoltaic (VIPV) Performance: A Review," *World Electric Vehicle Journal* 14, no. 6 (2023): 154.

12. U. Leopold, C. Braun, and P. Pinheiro, "An Interoperable Digital Twin to Simulate Spatio-Temporal Photovoltaic Power Output and Grid Congestion at Neighbourhood and City Levels in Luxembourg," *International Archives of Photogrammetry, Remote Sensing and Spatial Information Sciences* XLVIII-4/W7-2023 (2023): 95–100.

13. J. Ku, S.-M. Kim, and H.-D. Park, "Energy-Saving Path Planning Navigation for Solar-Powered Vehicles Considering Shadows," *Renewable Energy* 2024 (2024): 121424.

14. P. Bunme, H. Mizuno, T. Takashima, and T. Oozeki, "GIS-Based Solar Irradiance Estimation Method in Vehicle Integrated Photovoltaic," (2024), SSRN, under review.

15. S. Neven-du Mont, M. Heinrich, A. Pfreundt, C. Kutter, A. Tummalieh, and H. Neuhaus, "Energy Yield Modelling of 2D and 3D Curved Photovoltaic Modules," in *Proceedings of the 37th European Photovoltaic Solar Energy Conference and Exhibition*, (2020): 822–827.

16. Y. Ota, T. Masuda, K. Araki, and M. Yamaguchi, "Curve-Correction Factor for Characterization of the Output of a Three-Dimensional Curved Photovoltaic Module on a Car Roof," *Coatings* 8, no. 12 (2018): 432.

17. K. Araki, Y. Ota, and M. Yamaguchi, “Measurement and Modeling of 3D Solar Irradiance for Vehicle-Integrated Photovoltaic,” *Applied Sciences* 10, no. 3 (2020): 872.

18. Y. Ota, K. Araki, A. Nagaoka, and K. Nishioka, “Curve Correction of Vehicle-Integrated Photovoltaics Using Statistics on Commercial Car Bodies,” *Progress in Photovoltaics: Research and Applications* 30, no. 2 (2022): 152–163.

19. S. Matsushita, K. Araki, Y. Ota, and K. Nishioka, “Is a Double-Bubble Curved Surface With Excellent Aerodynamics Suitable for Vehicle-Integrated Photovoltaic (VIPV) Installation?,” in *Proceedings of the 40th European Photovoltaic Solar Energy Conference and Exhibition*, (2023): 20331–1–20331–5.

20. M. C. Brito, T. Santos, F. Moura, D. Pera, and J. Rocha, “Urban Solar Potential for Vehicle Integrated Photovoltaics,” *Transportation Research Part D: Transport and Environment* 94 (2021): 102810.

21. F. Karoui, B. Chambion, F. Claudon, and B. Commault, “Integrated Photovoltaics Potential for Passenger Cars: A Focus on the Sensitivity to Electrical Architecture Losses,” *Applied Sciences* 13, no. 14 (2023): 8373.

22. F. Karoui, F. Claudon, B. Chambion, S. Catellani, and B. Commault, “Estimation of Integrated Photovoltaics Potential for Solar City Bus in Different Climate Conditions in Europe,” *Journal of Physics: Conference Series* 2454, no. 1 (2023): 12007.

23. R. Núñez, Á. Muñoz, L. J. San José, J. Macías, R. Herrero, and I. Antón, “Estimation of Solar Resource for Vehicle-Integrated Photovoltaics in Urban Environments Using Image-Based Shade Detection,” *Optics Express* 31, no. 21 (2023): 34240–34251.

24. A. G. Evgenii Sovetkin and B. E. Pieters, “Improving Horizon Computation Algorithm With Quasirandom Sequences,” *International Journal of Geographical Information Science* 0, no. 0 (2024): 1–26.

25. E. Sovetkin, A. Gerber, and B. E. Pieters, “Fast Horizon Approximation: Impacts on Integrated Photovoltaic Irradiation Simulations,” *Solar RRL* 2024 (2024): 2400474.

26. B. Pieters, E. Sovetkin, and M. Gordon, “SSDP: Simple Sky Dome Projector,” (2024), github.com/IEK-5/SSDP.

27. US Department of the Interior (DOI), “RockyWeb: LIDAR Measurements,” (2023), rockyweb.usgs.gov/vdelivery/Datasets/Staged/Elevation/LPC/Projects/.

28. “Federal Office of Topography Swisstopo,” (2023), swisstopo.admin.ch/en/knowledge-facts/geoinformation/lidar-data.html.

29. “3D-Measurement Data in North Rhine-Westphalia,” (2023), bezreg-koeln.nrw.de/brk_internet/geobasis/hoehenmodelle/3d-messdaten/index.html.

30. “Accédez aux données open data du craig,” (2023), drive.opendata.craig.fr/s/opendata.

31. “Berlin, LIDAR Data,” (2023), fbinter.stadt-berlin.de/fb/berlin/service_intern.jsp?id=a_lod2@senstadt&type=FEED.

32. “Ficheros binarios del vuelo LIDAR 2017 de la comunidad autónoma del país vasco,” (2023), https://ftp.geo.euskadi.eus/lidar/.

33. “LiDAR 2019 - relevé 3d du territoire luxembourgeois,” (2023), data.public.lu/fr/datasets/lidar-2019-releve-3d-du-territoire-luxembourgeois.

34. “Nederland centrum voor geodesie en geo-informatica NCG,” (2023), geotiles.nl/AHN1/.

35. “Copernicus Open Access Hub,” (2023), scihub.copernicus.eu.

36. “Deutscher wetterdienst: CDC-OpenData Area,” (2024), opendata.dwd.de/climate_environment/CDC/.

37. M. Lefèvre, “CAMS Solar Radiation Products Regular Validation Report, Issue #32, Sept.–Nov. 2020,” 32. Copernicus Atmosphere Monitoring Service, (2021), minesparis-psl.hal.science/hal-03621889.

38. R. Peibst, H. Fischer, M. Brunner, et al., “Demonstration of Feeding Vehicle-Integrated Photovoltaic-Converted Energy Into the High-Voltage On-Board Network of Practical Light Commercial Vehicles for Range Extension,” *Solar RRL* 6, no. 5 (2022): 2100516.

39. N. Patel, R. Peibst, B. E. Pieters, E. Sovetkin, and A. Reinders, “Systems Analysis of an Onboard PV System on a Demonstrator Light Commercial Vehicle,” (2024), Under Review in Progress in Photovoltaics.

40. R. Perez, R. Seals, and J. Michalsky, “All-Weather Model for Sky Luminance Distribution-Preliminary Configuration and Validation,” *Solar Energy* 50, no. 3 (1993): 235–245.

41. OpenStreetMap Contributors, “Tag Highway: Roads and Road-Related Facilities,” (2024), https://taginfo.openstreetmap.org/keys/highway#overview.

42. “OpenStreetMap Data Extracts,” (2024), download.geofabrik.de/.

43. “3D Models for Free,” (2023), free3d.com/.

44. Blender Online Community, “Blender—A 3D Modelling and Rendering Package,” (2018), http://www.blender.org.

45. M. Šúri and J. Hofierka, “A New GIS-Based Solar Radiation Model and Its Application to Photovoltaic Assessments,” *Transactions in GIS* 8, no. 2 (2004): 175–190.

46. P. Fu and P. M. Rich, “Design and Implementation of the Solar Analyst: An ArcView Extension for Modeling Solar Radiation at Landscape Scales,” in *Proceedings of the 19th Annual Esri User Conference*, (1999), San Diego, USA.

47. B. Pieters, “FreeSPA: Free Implementation of NREL SPA,” (2023), github.com/IEK-5/SSDP.

48. S. Pal, A. Reinders, and R. Saive, “Simulation of Bifacial and Monofacial Silicon Solar Cell Short-Circuit Current Density Under Measured Spectro-Angular Solar Irradiance,” *IEEE Journal of Photovoltaics* 10, no. 6 (2020): 1803–1815.

49. “Hardware Configuration of the JUWELS Cluster Module,” (2024), apps.fz-juelich.de/jsc/hps/juwels/configuration.html.

50. E. Sovetkin, B. Pieters, and M. Gordon, “Data and Scripts for Reproducing Results in Paper “Non-Uniformity of Average Light Distribution on Vehicles' Bodies”,” (2024), https://figshare.com/s/13141e26acd3f73c810b.

51. B. Hagemeier, “HDF Cloud–Helmholtz Data Federation Cloud Resources at the Jülich Supercomputing Centre,” *Journal of Large-Scale Research Facilities* 5, no. FZJ-2020-00569 (2019): A137.